


 Cite this: *New J. Chem.*, 2023, 47, 3266

# Synthesis of SiO<sub>2</sub>@MnCo<sub>2</sub>O<sub>4</sub> core–shell nanorattles using layered double hydroxide precursors and studies on their peroxidase-like activity†

 Pankaj Rana  and Pethaiyan Jeevanandam \*

The current work demonstrates a simple soft chemical approach to synthesize SiO<sub>2</sub>@MnCo<sub>2</sub>O<sub>4</sub> core–shell nanorattles using SiO<sub>2</sub>@MnCo–LDH (layered double hydroxide) precursors. XRD analysis indicates the formation of MnCo<sub>2</sub>O<sub>4</sub> nanoparticles (NPs) on SiO<sub>2</sub> spheres. FESEM images show hierarchical flower-like MnCo<sub>2</sub>O<sub>4</sub> NPs on the surface of the SiO<sub>2</sub> spheres. TEM micrographs show the interstitial space between the core (SiO<sub>2</sub>) and the shell (MnCo<sub>2</sub>O<sub>4</sub>), indicating the core–shell nanorattle morphology of SiO<sub>2</sub>@MnCo<sub>2</sub>O<sub>4</sub>. BET adsorption–desorption isotherms of the SiO<sub>2</sub>@MnCo<sub>2</sub>O<sub>4</sub> core–shell nanorattles indicate their mesoporous nature with high surface area. Optical studies indicate O<sup>2–</sup> → Mn<sup>2+</sup> and O<sup>2–</sup> → Co<sup>3+</sup> charge-transfer transitions and d–d transition in pure MnCo<sub>2</sub>O<sub>4</sub> NPs and the SiO<sub>2</sub>@MnCo<sub>2</sub>O<sub>4</sub> core–shell nanorattles. XPS measurements indicate the presence of Si<sup>4+</sup>, Mn<sup>2+</sup>, Co<sup>2+</sup>, Mn<sup>3+</sup>, Co<sup>3+</sup>, and O<sup>2–</sup> in the SiO<sub>2</sub>@MnCo<sub>2</sub>O<sub>4</sub> core–shell nanorattles. The SiO<sub>2</sub>@MnCo<sub>2</sub>O<sub>4</sub> core–shell nanorattles show paramagnetic and superparamagnetic behavior at 300 K and 5 K, respectively. After characterization, the SiO<sub>2</sub>@MnCo<sub>2</sub>O<sub>4</sub> core–shell nanorattles were explored for peroxidase-like activity for the first time. The SiO<sub>2</sub>@MnCo<sub>2</sub>O<sub>4</sub> core–shell nanorattles act as a peroxidase nanozyme and exhibit better peroxidase-like activity than pure MnCo<sub>2</sub>O<sub>4</sub> NPs and horseradish peroxidase.

 Received 5th October 2022,  
 Accepted 9th January 2023

DOI: 10.1039/d2nj04901e

rsc.li/njc

## Introduction

Recently, core–shell NPs have received considerable attention due to their remarkable properties. Combining two different materials (core and shell) changes the properties of the original core and the shell.<sup>1</sup> Among core–shell NPs, core–shell nanorattles or yolk–shell nanoparticles possess interesting morphological features. Core–shell nanorattles or yolk–shell nanostructures have advantages because of their core@void@shell configuration. Core–shell nanorattles possess enhanced properties due to the void space between the core and the shell.<sup>1,2</sup> Core–shell nanorattles based on metal oxides have several promising applications such as in drug delivery, catalysis, sensing, Li-ion batteries, and adsorption.<sup>2,3</sup> Lee *et al.* have reported Au@SiO<sub>2</sub> yolk–shell structures as catalyst for the reduction of *p*-nitrophenol.<sup>4</sup> Kandula *et al.* have reported peroxidase-like activity of SiO<sub>2</sub>@Co<sub>3</sub>O<sub>4</sub> nanorattles.<sup>5</sup> Chen *et al.* have reported lithium storage properties of α-Fe<sub>2</sub>O<sub>3</sub>@SnO<sub>2</sub> nanorattles.<sup>6</sup> Rokicinska *et al.* have reported Co<sub>3</sub>O<sub>4</sub>@SiO<sub>2</sub>

core–shell nanorattles for catalytic combustion of toluene.<sup>7</sup> Hu *et al.* have reported α-Fe<sub>2</sub>O<sub>3</sub>@SiO<sub>2</sub> and SnO<sub>2</sub>@SiO<sub>2</sub> core–shell nanorattles as anticancer drug carriers.<sup>8</sup>

Silica (SiO<sub>2</sub>) is an amorphous insulator, which is stable at high temperatures and in water. The spherical morphology and porous nature of SiO<sub>2</sub> make it a good candidate as a core material for the synthesis of silica-based core–shell NPs/nanorattles.<sup>9</sup> SiO<sub>2</sub>-based nanorattles have been studied for various applications such as Co@SiO<sub>2</sub> core–shell nanorattles as catalysts,<sup>10</sup> α-Fe<sub>2</sub>O<sub>3</sub>@SiO<sub>2</sub> and SnO<sub>2</sub>@SiO<sub>2</sub> core–shell nanorattles as anticancer drug carriers,<sup>8</sup> SiO<sub>2</sub>@Co<sub>3</sub>O<sub>4</sub> core–shell nanorattles as nanozymes,<sup>5</sup> rattle-type gold nanorods/SiO<sub>2</sub> nanocomposites for chemo-photothermal therapy,<sup>11</sup> Au@SiO<sub>2</sub> yolk–shell nanostructures as catalyst for reduction of *p*-nitrophenol,<sup>4</sup> and Fe<sup>0</sup>@SiO<sub>2</sub> nanoparticles as catalyst for Fenton-like reaction.<sup>12</sup>

MnCo<sub>2</sub>O<sub>4</sub> is a spinel-type metal oxide in which Mn<sup>2+</sup> ions occupy octahedral (O<sub>h</sub>) sites, and Co<sup>2+</sup> and Co<sup>3+</sup> ions occupy both tetrahedral (T<sub>d</sub>) and O<sub>h</sub> sites.<sup>13</sup> Due to the high oxidation potential of cobalt and high electron transport ability of manganese, MnCo<sub>2</sub>O<sub>4</sub> exhibits exceptional electrochemical and physicochemical properties.<sup>14</sup> MnCo<sub>2</sub>O<sub>4</sub> nanoparticles are used in diverse applications such as asymmetric supercapacitors, anode materials in Li-ion batteries, photocatalysis, adsorption, and oxygen reduction.<sup>14–18</sup> MnCo<sub>2</sub>O<sub>4</sub>-based core–shell NPs have

Department of Chemistry, Indian Institute of Technology Roorkee, Roorkee-247667, India. E-mail: jeevafcy@iitr.ac.in; Fax: +91-1332-273560; Tel: +91-1332-285444

† Electronic supplementary information (ESI) available. See DOI: <https://doi.org/10.1039/d2nj04901e>

been used in different applications. For example, Wang *et al.* have reported  $\text{MnCo}_2\text{O}_4@ \text{MnCo}_2\text{S}_4$  core-shell nanostructures for asymmetric supercapacitors.<sup>19</sup> Zhao *et al.* have reported  $\text{MnCo}_2\text{O}_4@ \text{Ni}(\text{OH})_2$  core-shell flowers with ultrahigh specific capacitance.<sup>20</sup> Li *et al.* have reported  $\text{MnCo}_2\text{O}_4@ \text{NiCo}_2\text{O}_4$  core-shell NPs for dye-sensitized solar cells.<sup>21</sup> Sun *et al.* have reported  $\text{MnCo}_2\text{O}_4@ \text{C}$  core-shell nanowires for water splitting.<sup>22</sup> Zhao *et al.* have reported  $\text{Co}_3\text{O}_4@ \text{MnCo}_2\text{O}_4$  core-shell nanowire arrays for electrochemical energy storage.<sup>23</sup> Mehrez *et al.* have reported  $\text{MnCo}_2\text{O}_4@ \text{NiMoO}_4$  core-shell nanowire arrays for supercapacitor applications.<sup>24</sup>

Enzymes are biocatalysts that catalyze several biochemical reactions with high efficiency and selectivity.<sup>25</sup> Natural enzymes have several limitations. They have low stability, complex storage requirements, high cost, and less adaptability under harsh environmental conditions.<sup>26</sup> To overcome the drawbacks of natural enzymes, nanomaterials have been used as an alternative. Metal oxide-based nanozymes have been explored to mimic different natural enzymes such as peroxidase, ferroxidase, catalase, and superoxide dismutase.<sup>26,27</sup> Horseradish peroxidase oxidizes different substrates in the presence of hydrogen peroxide.<sup>28</sup> In the literature, different metal oxide-based nanozymes have been used as a peroxidase mimic. For example, Chen *et al.* have reported CuO nanoparticles for peroxidase-like activity.<sup>29</sup> Fu *et al.* have investigated the peroxidase-like activity of  $\text{Fe}_3\text{O}_4$  nanoparticles for cancer therapy.<sup>30</sup> Gao *et al.* have reported  $\text{MnCo}_2\text{O}_4$  nanofibers as a catalyst for peroxidase-like activity.<sup>31</sup> Ma *et al.* have reported photoinduced peroxidase-like activity of  $\text{NiCo}_2\text{O}_4@ \text{MnO}_2$  nanozymes.<sup>32</sup>

Multi-functional core-shell NPs and nanorattles have been synthesized using various soft chemical synthesis routes. For example, Wang *et al.* have reported the synthesis of  $\text{MnCo}_2\text{O}_4@ \text{MnCo}_2\text{S}_4$  core-shell nanostructures using the hydrothermal method.<sup>19</sup> Zhao *et al.* have reported the synthesis of  $\text{MnCo}_2\text{O}_4@ \text{Ni}(\text{OH})_2$  core-shell flowers using homogeneous precipitation.<sup>20</sup> Mehrez *et al.* have reported the synthesis of  $\text{MnCo}_2\text{O}_4@ \text{NiMoO}_4$  core-shell nanowires using hydrothermal method.<sup>24</sup> Zhang *et al.* have reported the preparation of  $\text{Co}@ \text{CoO}$  core-shell nanocomposites using solvothermal method.<sup>33</sup> Gao *et al.* have reported the synthesis of  $\text{NiCo}_2\text{O}_4@ \text{SnO}_2$  hetero-nanostructures using the hydrothermal method.<sup>34</sup> Kandula *et al.* have reported the preparation of  $\text{SiO}_2@ \text{NiCo}_2\text{O}_4$  core-shell nanorattles using homogeneous precipitation.<sup>35</sup>

The current work demonstrates a reliable and cost-effective synthetic strategy to prepare  $\text{SiO}_2@ \text{MnCo}_2\text{O}_4$  nanorattles *via* calcination of  $\text{SiO}_2@ \text{MnCo-LDH}$  precursors at 500 °C. The  $\text{MnCo}_2\text{O}_4$  nanoparticles deposit on the surface of the  $\text{SiO}_2$  spheres creating a hollow space (void) between the core and shell. The influence of  $[\text{Mn}^{2+} : \text{Co}^{2+}]$  ratio on the thickness of the  $\text{MnCo}_2\text{O}_4$  shell and void distance between the core ( $\text{SiO}_2$ ) and shell ( $\text{MnCo}_2\text{O}_4$ ) has been investigated. The  $\text{SiO}_2@ \text{MnCo}_2\text{O}_4$  core-shell nanorattles exhibit better peroxidase-like activity than pure  $\text{MnCo}_2\text{O}_4$  NPs using 3,3',5,5'-tetramethylbenzidine (TMB) as the substrate. To the best of the authors' knowledge, there is no report on the synthesis of  $\text{SiO}_2@ \text{MnCo}_2\text{O}_4$  core-shell nanorattles and the  $\text{SiO}_2@ \text{MnCo}_2\text{O}_4$  nanorattles have been employed as a peroxidase mimic for the first time.

## Experimental

### Reagents

Tetraethyl orthosilicate (98%, Sigma-Aldrich), ammonia solution (25%, Rankem),  $\text{Mn}(\text{NO}_3)_2 \cdot 4\text{H}_2\text{O}$  (97%, Sigma-Aldrich),  $\text{Co}(\text{NO}_3)_2 \cdot 6\text{H}_2\text{O}$  (98%, Merck), urea (99.5%, Rankem), 3,3',5,5'-tetramethylbenzidine (98%, Spectrochem Chemicals), ethanol (99.9%, Changshu Hongsheng Fine Chemical Co., Ltd.), and  $\text{H}_2\text{O}_2$  (30%, Rankem, AR). All the chemicals were used as received.

### Synthesis of silica microspheres

$\text{SiO}_2$  microspheres were synthesized using a previously reported Stöber's method.<sup>36</sup> About 3.7 mL of tetraethyl orthosilicate was added (dropwise) to a mixture of 88 mL of EtOH and 12 mL of  $\text{NH}_4\text{OH}$  solution with constant stirring. The reaction mixture was continuously stirred at RT for 24 h to get a white-colored product. The product was centrifuged, washed with EtOH, and dried in an oven overnight at 70 °C.

### Synthesis of $\text{SiO}_2@ \text{MnCo}_2\text{O}_4$ core-shell nanorattles

First,  $\text{SiO}_2@ \text{MnCo-LDH}$  precursors were prepared using different molar ratios of  $[\text{Mn}^{2+} : \text{Co}^{2+}]$ . The synthetic parameters for the  $\text{SiO}_2@ \text{MnCo-LDH}$  precursors are given in Table 1. In a typical synthetic experiment,  $\text{Mn}(\text{NO}_3)_2 \cdot 4\text{H}_2\text{O}$ ,  $\text{Co}(\text{NO}_3)_2 \cdot 6\text{H}_2\text{O}$  and urea were dissolved in 100 mL of distilled water in a 250 mL beaker. Then,  $\text{SiO}_2$  microspheres (100 mg) were dispersed in the aqueous solution and sonicated for 10 minutes. The contents were heated at 85 °C for six hours with constant stirring. The product was collected by centrifuging and washing with deionized water and ethanol, followed by drying in an oven at 60 °C for about 12 h. The as-prepared  $\text{SiO}_2@ \text{MnCo-LDH}$  precursors were calcined at 500 °C (in a muffle furnace) for 3 h (heating rate = 2 °C per minute) in air to get the corresponding  $\text{SiO}_2@ \text{MnCo}_2\text{O}_4$  samples. The as-prepared  $\text{SiO}_2@ \text{MnCo-LDH}$  precursors, prepared using different molar ratios of  $[\text{Mn}^{2+} : \text{Co}^{2+}]$  (0.25:0.5, 0.5:1, and 1:2), will henceforth be referred to as  $\text{SiO}_2@ \text{MnCo-LDH-0.25}$ ,  $\text{SiO}_2@ \text{MnCo-LDH-0.5}$ , and  $\text{SiO}_2@ \text{MnCo-LDH-1}$ , respectively. The  $\text{SiO}_2@ \text{MnCo}_2\text{O}_4$  samples, obtained on calcination, will henceforth be referred to as  $\text{SiO}_2@ \text{MnCo}_2\text{O}_4-0.25$ ,  $\text{SiO}_2@ \text{MnCo}_2\text{O}_4-0.5$ , and  $\text{SiO}_2@ \text{MnCo}_2\text{O}_4-1$ , respectively.

### Peroxidase-like activity and kinetic analysis

The peroxidase-like activity of the  $\text{SiO}_2@ \text{MnCo}_2\text{O}_4$  nanorattles was studied utilizing tetramethylbenzidine (TMB) and  $\text{H}_2\text{O}_2$  as a substrate, and oxidizing agent, respectively. About 300  $\mu\text{L}$  of 3 mM TMB solution (DMSO) and 31  $\mu\text{L}$  of 100 mM  $\text{H}_2\text{O}_2$  were mixed with 3 mL of acetate buffer (0.1 M, pH = 5). Then, 30  $\mu\text{L}$

**Table 1** Synthetic details of  $\text{SiO}_2@ \text{MnCo-LDH}$  samples and their nomenclature

Sample code	$[\text{Mn}^{2+}] : [\text{Co}^{2+}]$	$\text{SiO}_2$ (mg)	Urea (g)	Temperature (°C)	Time (h)
$\text{SiO}_2@ \text{MnCo-LDH-0.25}$	0.25 : 0.5	100	1.0	85	6
$\text{SiO}_2@ \text{MnCo-LDH-0.5}$	0.5 : 1	100	1.0	85	6
$\text{SiO}_2@ \text{MnCo-LDH-1}$	1 : 2	100	1.0	85	6
$\text{MnCo-LDH}$	1 : 2	—	1.0	85	6

of catalyst dispersion (1 mg of  $\text{SiO}_2@\text{MnCo}_2\text{O}_4$  catalyst dispersed by sonication in 1 mL of deionized water) was added to the reaction mixture. The absorbance values ( $@\lambda_{\text{max}} = 652 \text{ nm}$ ) of the reaction mixture were measured using a UV-Vis spectrophotometer (Shimadzu UV-2600) up to 10 minutes. Kinetic experiments were performed by changing various experimental parameters, such as TMB concentration (0.05 to 0.5 mM), pH (2–12), catalyst dose (5–60  $\mu\text{L}$ ), and  $\text{H}_2\text{O}_2$  concentration (5–200 mM). The kinetic parameters ( $K_m$  and  $V_{\text{max}}$ ) were estimated using the Michaelis–Menten equation and Lineweaver–Burk reciprocal plots.<sup>32</sup> The Michaelis–Menten equation is as follows.

$$1/V = (K_m/V_{\text{max}}) (1/[S]) + 1/V_{\text{max}}$$

where  $K_m$  and  $V_{\text{max}}$  denote the Michaelis–Menten constant and maximum reaction velocity, respectively.  $V$  and  $[S]$  denote reaction velocity and concentration of the substrate (TMB), respectively.

Terephthalic acid was employed as a probe molecule to prove the role of hydroxyl radicals in the peroxidase-like activity of the  $\text{SiO}_2@\text{MnCo}_2\text{O}_4$  nanorattles. In a cuvette, buffer (3 mL, pH = 5) and 100 mM  $\text{H}_2\text{O}_2$  (31  $\mu\text{L}$ ) were mixed, followed by the addition of 30  $\mu\text{L}$  of catalyst dispersion ( $\text{SiO}_2@\text{MnCo}_2\text{O}_4$ ). The reaction mixture was then treated with 0.5 mL of aqueous terephthalic acid solution (0.5 mM). A spectrofluorometer (Horiba Scientific, Fluoromax-4) was used to measure the PL spectra of the solution ( $\lambda_{\text{exc}} = 315 \text{ nm}$ ) up to 50 minutes.

### Characterization

Powder X-ray diffraction patterns of all the samples were recorded using a Bruker AXS D8 Advance powder X-ray diffractometer ( $\text{Cu-K}_\alpha$ ,  $\lambda = 1.5406 \text{ \AA}$ , scan speed =  $1^\circ \text{ min}^{-1}$ ) in the  $2\theta$  range of  $5^\circ$  to  $90^\circ$ . FT-IR spectra of the samples (using KBr pellets) were recorded using a Thermo Nicolet Nexus FT-IR spectrophotometer ( $4000$  to  $400 \text{ cm}^{-1}$ ). A PerkinElmer Pyris Diamond instrument was used to perform thermal gravimetric analysis (TGA) of the  $\text{SiO}_2@\text{MnCo-LDH}$  precursors; the precursors were heated at a rate of  $10^\circ \text{ C min}^{-1}$  in air between  $30^\circ \text{ C}$  and  $1000^\circ \text{ C}$ . A Carl Zeiss Gemini scanning electron microscope (operating voltage = 20 kV) was used to examine the morphology of the samples. For elemental analysis, the SEM attached with an EDXA unit was employed. The core-shell nanorattles were imaged using a FEI Tecnai G2 20S-TWIN transmission electron microscope (operating voltage = 200 kV). Using a Quantum Design MPMS3 superconducting quantum interference device, the magnetic properties of the  $\text{SiO}_2@\text{MnCo}_2\text{O}_4$  core-shell nanorattles were studied. X-ray photoelectron spectroscopy (XPS) measurements were performed on a Physical Electronics make (PHI 5000 Versa Probe III) spectrometer ( $\text{Al-K}_\alpha$  radiation, energy = 1486.6 eV). Physisorption of  $\text{N}_2$  at 77 K was used to determine surface area of the  $\text{SiO}_2@\text{MnCo}_2\text{O}_4$  core-shell nanorattles using a Quantachrome BET surface area analyzer (model = Nova 2200e).

## Results and discussion

The results related to  $\text{SiO}_2@\text{MnCo-LDH}$  precursors are given in the ESI.† The results related to  $\text{SiO}_2@\text{MnCo}_2\text{O}_4$  core-shell nanorattles are discussed below.

### $\text{SiO}_2@\text{MnCo}_2\text{O}_4$ core-shell nanorattles

**Phase analysis.** Pure  $\text{MnCo}_2\text{O}_4$  NPs and  $\text{SiO}_2@\text{MnCo}_2\text{O}_4$  core-shell NPs were obtained on calcination of  $\text{MnCo-LDH}$  and  $\text{SiO}_2@\text{MnCo-LDH}$  samples at  $500^\circ \text{ C}$ , respectively. The XRD patterns of the  $\text{MnCo}_2\text{O}_4$  and  $\text{SiO}_2@\text{MnCo}_2\text{O}_4$  samples are shown in Fig. 1. The XRD pattern of  $\text{MnCo}_2\text{O}_4$  matches with the pattern of cubic  $\text{MnCo}_2\text{O}_4$  (JCPDS file no. 23-1237). The peaks observed at  $2\theta = 18.1^\circ, 30.4^\circ, 35.9^\circ, 43.9^\circ, 53.5^\circ, 58.4^\circ,$  and  $64.5^\circ$  are ascribed to (111), (220), (311), (400), (422), (511), and (440) reflections of cubic  $\text{MnCo}_2\text{O}_4$ . The XRD patterns of the  $\text{SiO}_2@\text{MnCo}_2\text{O}_4-0.25$  and  $\text{SiO}_2@\text{MnCo}_2\text{O}_4-0.5$  samples show peaks at  $2\theta = 35.9^\circ$  and  $64.5^\circ$  attributed to the (311) and (440) planes of  $\text{MnCo}_2\text{O}_4$ .

The XRD pattern of  $\text{SiO}_2@\text{MnCo}_2\text{O}_4-1$  shows peaks at  $2\theta = 18.1^\circ, 30.2^\circ, 35.9^\circ, 43.7^\circ, 58.3^\circ,$  and  $64.3^\circ$  due to (111), (220), (311), (400), (511), and (440) reflections of  $\text{MnCo}_2\text{O}_4$ . The estimated crystallite size (using the Scherrer formula) of  $\text{MnCo}_2\text{O}_4$  are 9.3 nm, 6.4 nm, 3.5 nm, and 7.5 nm for  $\text{MnCo}_2\text{O}_4$ ,  $\text{SiO}_2@\text{MnCo}_2\text{O}_4-0.25$ ,  $\text{SiO}_2@\text{MnCo}_2\text{O}_4-0.5$ , and  $\text{SiO}_2@\text{MnCo}_2\text{O}_4-1$ , respectively. The  $\text{SiO}_2@\text{MnCo}_2\text{O}_4$  samples possess smaller crystallites of  $\text{MnCo}_2\text{O}_4$  compared to pristine  $\text{MnCo}_2\text{O}_4$  NPs.

### FT-IR analysis

Fig. S5 (ESI†) displays the FT-IR spectra of  $\text{MnCo}_2\text{O}_4$  and  $\text{SiO}_2@\text{MnCo}_2\text{O}_4$  samples ( $\text{SiO}_2@\text{MnCo}_2\text{O}_4-0.25$ ,  $\text{SiO}_2@\text{MnCo}_2\text{O}_4-0.5$ , and  $\text{SiO}_2@\text{MnCo}_2\text{O}_4-1$ ). The IR spectra of all the samples exhibit bands at about  $3438 \text{ cm}^{-1}$ , and  $1637 \text{ cm}^{-1}$  assigned to stretching and bending vibrational modes of physisorbed  $\text{H}_2\text{O}$  molecules. The IR spectrum of  $\text{MnCo}_2\text{O}_4$  shows IR bands around  $659 \text{ cm}^{-1}$  and  $568 \text{ cm}^{-1}$  attributed to stretching vibration of Co–O and Mn–O bonds, respectively.<sup>14</sup> The IR spectra of all the  $\text{SiO}_2@\text{MnCo}_2\text{O}_4$  samples display characteristic bands of  $\text{SiO}_2$  at  $1105 \text{ cm}^{-1}$  and  $486 \text{ cm}^{-1}$  due to  $\nu(\text{Si-O-Si})$  and  $\delta(\text{Si-O-Si})$ , respectively.<sup>5</sup> In the IR spectra of the  $\text{SiO}_2@\text{MnCo}_2\text{O}_4$  samples, the bands observed at about  $660 \text{ cm}^{-1}$  and  $565 \text{ cm}^{-1}$  are assigned to the stretching vibrations of Co–O and Mn–O bonds, respectively.<sup>14</sup>

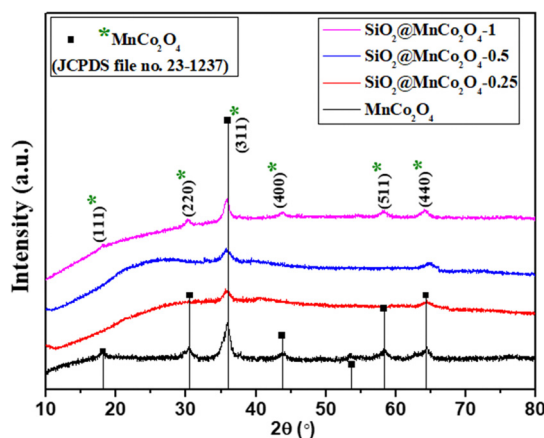


Fig. 1 XRD patterns of  $\text{MnCo}_2\text{O}_4$  and  $\text{SiO}_2@\text{MnCo}_2\text{O}_4$  samples obtained by calcination of LDH precursors (Table 1) at  $500^\circ \text{ C}$ .

### Morphological studies and elemental analysis

Fig. 2(a–d) displays FESEM images of pure  $\text{MnCo}_2\text{O}_4$  and  $\text{SiO}_2@\text{MnCo}_2\text{O}_4$  samples ( $\text{SiO}_2@\text{MnCo}_2\text{O}_4$ -0.25,  $\text{SiO}_2@\text{MnCo}_2\text{O}_4$ -0.5, and  $\text{SiO}_2@\text{MnCo}_2\text{O}_4$ -1). The FESEM image of pure  $\text{MnCo}_2\text{O}_4$ , (Fig. 2(a)) shows nanosheets (flake-like structures). The FESEM images of the  $\text{SiO}_2@\text{MnCo}_2\text{O}_4$  samples (Fig. 2(b–d)) show that the  $\text{SiO}_2$  spheres are uniformly covered with  $\text{MnCo}_2\text{O}_4$  nanoparticles. Table S4 (ESI<sup>†</sup>) summarizes the EDX analysis results for all  $\text{SiO}_2@\text{MnCo}_2\text{O}_4$  samples (after calcination at 500 °C). The results indicate that Si, Mn, Co, and O are present uniformly in all the  $\text{SiO}_2@\text{MnCo}_2\text{O}_4$  core-shell NPs. The weight % of Mn and Co in the  $\text{SiO}_2@\text{MnCo}_2\text{O}_4$  samples varies according to the  $[\text{Mn}^{2+}]:[\text{Co}^{2+}]$  ratio used during the synthesis of their precursors ( $\text{SiO}_2@\text{MnCo-LDH}$ ).

Fig. 3(a–e) shows the TEM images of  $\text{SiO}_2$ , pristine  $\text{MnCo}_2\text{O}_4$ , and  $\text{SiO}_2@\text{MnCo}_2\text{O}_4$  samples ( $\text{SiO}_2@\text{MnCo}_2\text{O}_4$ -0.25,  $\text{SiO}_2@\text{MnCo}_2\text{O}_4$ -0.5, and  $\text{SiO}_2@\text{MnCo}_2\text{O}_4$ -1). A summary of the TEM results is given in Table 2. The TEM image of  $\text{SiO}_2$  (Fig. 3(a)) shows spherical particles with mean diameter of  $175 \pm 14$  nm. Fig. 3(b) displays the TEM image of pristine  $\text{MnCo}_2\text{O}_4$ , showing its flake-like morphology (nanosheet). The mean thickness of  $\text{MnCo}_2\text{O}_4$  nanosheets is  $9.3 \pm 3.6$  nm. The TEM images (Fig. 3(c–e)) of  $\text{SiO}_2@\text{MnCo}_2\text{O}_4$  samples ( $\text{SiO}_2@\text{MnCo}_2\text{O}_4$ -0.25,  $\text{SiO}_2@\text{MnCo}_2\text{O}_4$ -0.5, and  $\text{SiO}_2@\text{MnCo}_2\text{O}_4$ -1) show interstitial space (void) between the core ( $\text{SiO}_2$ ) and the shell ( $\text{MnCo}_2\text{O}_4$ ). Such nanoparticles are known in the literature as core-shell nanorattles or nanoparticles with yolk-shell morphology.<sup>37,38</sup> The TEM images also reveal that the  $\text{MnCo}_2\text{O}_4$  shell has a porous flower-like structure. From Table 2, it is observed that the mean size of the  $\text{SiO}_2$  core in the  $\text{SiO}_2@\text{MnCo}_2\text{O}_4$  core-shell nanorattles varies from  $171 \pm 13$  nm to  $190 \pm 15$  nm. The mean thickness of the  $\text{MnCo}_2\text{O}_4$  shell lies in the range of  $38 \pm 8$  nm to  $60 \pm 12$  nm. The average void distance between the  $\text{SiO}_2$  core and  $\text{MnCo}_2\text{O}_4$  shell varies from  $16 \pm 3$  nm to  $30 \pm 6$  nm. The mean thickness of the nanosheets of  $\text{MnCo}_2\text{O}_4$  (shell) in the  $\text{SiO}_2@\text{MnCo}_2\text{O}_4$  core-shell nanorattles varies from  $2.6 \pm 0.9$  nm to  $3.3 \pm 0.4$  nm. The synthetic conditions play an

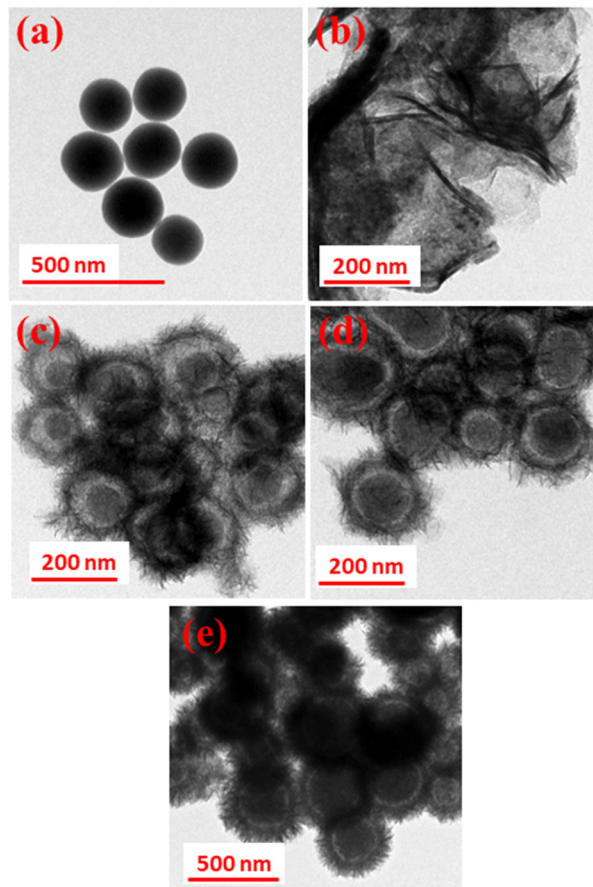


Fig. 3 TEM images of (a)  $\text{SiO}_2$ , (b)  $\text{MnCo}_2\text{O}_4$ , (c)  $\text{SiO}_2@\text{MnCo}_2\text{O}_4$ -0.25, (d)  $\text{SiO}_2@\text{MnCo}_2\text{O}_4$ -0.5 and (e)  $\text{SiO}_2@\text{MnCo}_2\text{O}_4$ -1 core-shell samples calcined at 500 °C.

Table 2 Summary of TEM results of  $\text{SiO}_2@\text{MnCo}_2\text{O}_4$  core-shell nanorattles

Sample code	Core size (nm)	Shell thickness (nm)	Void distance (nm)	Flake thickness in the shell (nm)
$\text{SiO}_2@\text{MnCo}_2\text{O}_4$ -0.25	$182 \pm 13$	$38 \pm 8$	$30 \pm 6$	$2.6 \pm 0.9$
$\text{SiO}_2@\text{MnCo}_2\text{O}_4$ -0.5	$171 \pm 13$	$41 \pm 10$	$16 \pm 3$	$3.2 \pm 0.6$
$\text{SiO}_2@\text{MnCo}_2\text{O}_4$ -1	$190 \pm 15$	$60 \pm 12$	$22 \pm 4$	$3.3 \pm 0.4$

important role in the nanorattle formation. As the concentration (molar ratio) of metal salts used during the synthesis of  $\text{SiO}_2@\text{MnCo-LDH}$  precursors (*i.e.*  $\text{Mn}(\text{NO}_3)_2 \cdot 4\text{H}_2\text{O}$  and  $\text{Co}(\text{NO}_3)_2 \cdot 6\text{H}_2\text{O}$ ) increases from 0.25:0.5 to 1:2, more  $\text{MnCo}_2\text{O}_4$  NPs are formed on the surface of the  $\text{SiO}_2$  spheres, which leads to a thick coating of  $\text{MnCo}_2\text{O}_4$  NPs on the surface of the  $\text{SiO}_2$  spheres. When lower concentration of metal salts is used, a thin coating of  $\text{MnCo}_2\text{O}_4$  NPs occurs and thus in the  $\text{SiO}_2@\text{MnCo}_2\text{O}_4$ -0.25 sample, the thin coating of  $\text{MnCo}_2\text{O}_4$  leads to a good TEM image. EDS mapping and elemental line profiles of  $\text{SiO}_2@\text{MnCo}_2\text{O}_4$  from TEM measurements were done and the results are shown in Fig. S6 and S7 (ESI<sup>†</sup>). The EDS elemental mapping images and elemental line profile of the  $\text{SiO}_2@\text{MnCo}_2\text{O}_4$  core-shell nanorattles indicate

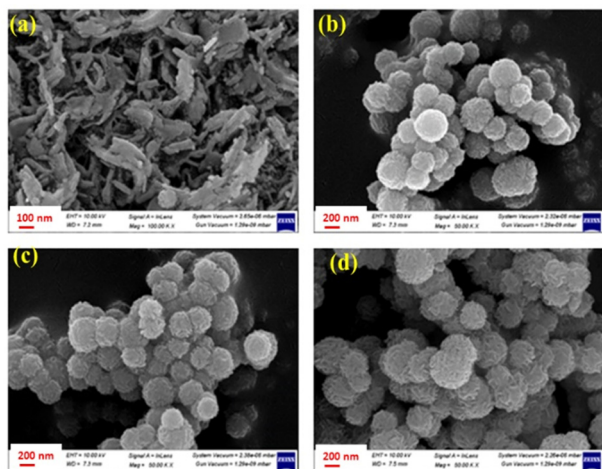


Fig. 2 FE-SEM images of (a)  $\text{MnCo}_2\text{O}_4$ , (b)  $\text{SiO}_2@\text{MnCo}_2\text{O}_4$ -0.25, (c)  $\text{SiO}_2@\text{MnCo}_2\text{O}_4$ -0.5, and (d)  $\text{SiO}_2@\text{MnCo}_2\text{O}_4$ -1 core-shell samples calcined at 500 °C.

uniform distribution of elements (Si, Mn, Co and O) in the  $\text{SiO}_2@\text{MnCo}_2\text{O}_4$  core-shell nanorattles. The line scan EDS images show that the Mn and Co content is more towards the edge of the spherical particles and the Si content is more in the center of the particles. This suggests coating of  $\text{MnCo}_2\text{O}_4$  on the  $\text{SiO}_2$  spheres.

The SAED patterns of pure  $\text{MnCo}_2\text{O}_4$  NPs and  $\text{SiO}_2@\text{MnCo}_2\text{O}_4$  samples ( $\text{SiO}_2@\text{MnCo}_2\text{O}_4-0.25$ ,  $\text{SiO}_2@\text{MnCo}_2\text{O}_4-0.5$ , and  $\text{SiO}_2@\text{MnCo}_2\text{O}_4-1$ ) are displayed in Fig. S8(a-d) (ESI<sup>†</sup>). The SAED pattern of pure  $\text{MnCo}_2\text{O}_4$  (Fig. S8(a), ESI<sup>†</sup>) shows rings which indicate the polycrystalline nature of the  $\text{MnCo}_2\text{O}_4$  NPs. The observed rings are attributed to (220), (311), (400), (422), and (440) reflections of cubic  $\text{MnCo}_2\text{O}_4$ . The SAED patterns of  $\text{SiO}_2@\text{MnCo}_2\text{O}_4-0.25$ ,  $\text{SiO}_2@\text{MnCo}_2\text{O}_4-0.5$ , and  $\text{SiO}_2@\text{MnCo}_2\text{O}_4-1$  core-shell nanorattles (Fig. S8(b-d), ESI<sup>†</sup>) also show rings, which suggests the polycrystalline nature of all the  $\text{SiO}_2@\text{MnCo}_2\text{O}_4$  nanorattles. The observed rings correspond to the (311) and (422) planes of cubic  $\text{MnCo}_2\text{O}_4$ .

### BET surface area analysis

BET surface area measurements were carried out to determine the surface area, pore size, and pore volume of the  $\text{SiO}_2@\text{MnCo}_2\text{O}_4$  core-shell nanorattles.  $\text{SiO}_2$  and  $\text{MnCo}_2\text{O}_4$  nanoparticles exhibit a surface area of  $88 \text{ m}^2 \text{ g}^{-1}$  and  $79 \text{ m}^2 \text{ g}^{-1}$ , respectively. The core-shell nanorattles ( $\text{SiO}_2@\text{MnCo}_2\text{O}_4-0.25$ ,  $\text{SiO}_2@\text{MnCo}_2\text{O}_4-0.5$ , and  $\text{SiO}_2@\text{MnCo}_2\text{O}_4-1$ ) exhibit surface area of  $278 \text{ m}^2 \text{ g}^{-1}$ ,  $302 \text{ m}^2 \text{ g}^{-1}$ , and  $356 \text{ m}^2 \text{ g}^{-1}$ , respectively. The higher surface area of the  $\text{SiO}_2@\text{MnCo}_2\text{O}_4$  nanorattles is attributed to the void space between the core ( $\text{SiO}_2$ ) and the shell ( $\text{MnCo}_2\text{O}_4$ ). Adsorption-desorption isotherms were recorded for pure  $\text{MnCo}_2\text{O}_4$  nanoparticles and  $\text{SiO}_2@\text{MnCo}_2\text{O}_4-1$ . As shown in Fig. S9(a) (ESI<sup>†</sup>), the adsorption-desorption isotherm of the  $\text{MnCo}_2\text{O}_4$  nanoparticles shows the characteristics of a porous material with open wedge pores. The adsorption-desorption isotherm of  $\text{SiO}_2@\text{MnCo}_2\text{O}_4-1$  (Fig. S9(b), ESI<sup>†</sup>) matches with a type IV isotherm.<sup>39</sup> The  $\text{MnCo}_2\text{O}_4$  nanoparticles exhibit an average pore size and pore volume of 6.2 nm and  $0.12 \text{ cm}^3 \text{ g}^{-1}$ , respectively. The  $\text{SiO}_2@\text{MnCo}_2\text{O}_4-1$  exhibits an average pore size and pore volume of 5.0 nm and  $0.44 \text{ cm}^3 \text{ g}^{-1}$ , respectively.

### Mechanism of formation of $\text{SiO}_2@\text{MnCo}_2\text{O}_4$ core-shell nanorattles

Fig. S10 (ESI<sup>†</sup>) shows the proposed mechanism of formation of  $\text{SiO}_2@\text{MnCo}_2\text{O}_4$  core-shell nanorattles. In the first step,  $\text{Mn}^{2+}$  and  $\text{Co}^{2+}$  ions from the aqueous solution attach to the OH groups present on the surface of the  $\text{SiO}_2$  spheres *via* electrostatic interaction. At  $85^\circ\text{C}$ , hydrolysis of urea leads to the production of  $\text{NH}_4^+$  and  $\text{OH}^-$  ions. The  $\text{OH}^-$  ions react with  $\text{Mn}^{2+}$  and  $\text{Co}^{2+}$  ions present on the surface of  $\text{SiO}_2$  forming  $\text{MnCo-LDH}$  *via* nucleation and coalescence processes. Finally, flower-like structures consisting of  $\text{MnCo-LDH}$  nanosheets are formed on the surface of the  $\text{SiO}_2$  spheres *via* Ostwald ripening.<sup>40,41</sup> The flower-like  $\text{SiO}_2@\text{MnCo-LDH}$  precursors are converted into  $\text{SiO}_2@\text{MnCo}_2\text{O}_4$  core-shell nanorattles *via* calcination at  $500^\circ\text{C}$  with retention of the morphology.

Time-dependent TEM studies were carried out to understand better the formation of  $\text{SiO}_2@\text{MnCo-LDH}$  nanorattles. The TEM images of  $\text{SiO}_2@\text{MnCo-LDH-0.25}$  recorded after different reaction times (1 h, 2 h, 3 h, 4 h, and 6 h) are shown in Fig. S11 (ESI<sup>†</sup>). After a reaction time of 1 h,  $\text{MnCo-LDH}$  crystallites are loosely attached on the outer surface of the  $\text{SiO}_2$  spheres. These  $\text{MnCo-LDH}$  crystallites act as seed for the nucleation and recrystallization. As the reaction progresses (2 h, 4 h), Ostwald ripening (inside-out) dominates and smaller crystallites of  $\text{MnCo-LDH}$  present in the interior region dissolve, which initiates the hollowing process. Finally, after 6 h, a close-packed  $\text{MnCo-LDH}$  shell is formed on the surface of the  $\text{SiO}_2$  spheres with a void space between the core and shell.  $\text{SiO}_2@\text{MnCo}_2\text{O}_4$  core-shell nanorattles are obtained on calcination of  $\text{SiO}_2@\text{MnCo-LDH}$  at  $500^\circ\text{C}$  with the retention of the morphological features of the LDH precursor.

### Optical properties of $\text{SiO}_2@\text{MnCo}_2\text{O}_4$ core-shell nanorattles

The optical properties of  $\text{MnCo}_2\text{O}_4$  nanoparticles and  $\text{SiO}_2@\text{MnCo}_2\text{O}_4$  core-shell nanorattles were studied using UV-Vis diffuse reflectance spectroscopy (DRS). The UV-Vis DRS spectra of the  $\text{MnCo}_2\text{O}_4$  nanoparticles and  $\text{SiO}_2@\text{MnCo}_2\text{O}_4$  core-shell nanorattles are shown in Fig. S12 (ESI<sup>†</sup>). The DRS spectra of the  $\text{MnCo}_2\text{O}_4$  NPs and  $\text{SiO}_2@\text{MnCo}_2\text{O}_4$  nanorattles show broad bands at 250 nm and 470 nm, attributed to  $\text{O}^{2-} \rightarrow \text{Mn}^{2+}$  and  $\text{O}^{2-} \rightarrow \text{Co}^{3+}$  charge-transfer transitions of  $\text{MnCo}_2\text{O}_4$ , respectively.<sup>43,44</sup> The DRS spectra of all the samples exhibit a broad band at about 738 nm due to d-d transitions of  $\text{Mn}^{2+}$  and  $\text{Co}^{3+}$  of  $\text{MnCo}_2\text{O}_4$  NPs.<sup>42,43</sup>

### XPS analysis

The oxidation states of Si, Mn, Co, and O in  $\text{SiO}_2$ ,  $\text{MnCo}_2\text{O}_4$  NPs and  $\text{SiO}_2@\text{MnCo}_2\text{O}_4-1$  nanorattles were determined using XPS analysis.

Fig. S13 (ESI<sup>†</sup>) displays the XPS spectrum of  $\text{SiO}_2$ . The Si 2p spectrum of  $\text{SiO}_2$  shows a peak at 103.8 eV, indicating the existence of  $\text{Si}^{4+}$ . The O 1s spectrum of  $\text{SiO}_2$  shows peaks at 532.7 eV and 533.8 eV, indicating the existence of lattice oxygen and surface hydroxyl oxygen in  $\text{SiO}_2$ , respectively.<sup>44</sup> Fig. 4(a and b) shows the XPS spectra of pure  $\text{MnCo}_2\text{O}_4$  NPs and  $\text{SiO}_2@\text{MnCo}_2\text{O}_4-1$ . The Mn 2p spectrum of pure  $\text{MnCo}_2\text{O}_4$  NPs (Fig. 4(a)) shows peaks due to Mn 2p<sub>3/2</sub> (642.1 eV ( $\text{Mn}^{2+}$ ) and 643.5 eV ( $\text{Mn}^{3+}$ ) and Mn 2p<sub>1/2</sub> (654.0 eV). The Co 2p spectrum of  $\text{MnCo}_2\text{O}_4$  NPs (Fig. 4(a)) shows peaks due to Co 2p<sub>3/2</sub> (780.1 eV ( $\text{Co}^{2+}$ ) and 782.1 eV ( $\text{Co}^{3+}$ ) and Co 2p<sub>1/2</sub> (795.2 eV ( $\text{Co}^{2+}$ ) and 797.3 eV ( $\text{Co}^{3+}$ )). The peaks observed at 788.0 eV and 803.8 eV correspond to satellite peaks. The O 1s spectrum of pure  $\text{MnCo}_2\text{O}_4$  NPs shows peaks at 530.1 eV and 531.9 eV, assigned to lattice oxygen of  $\text{MnCo}_2\text{O}_4$  and surface hydroxyl oxygen, respectively.<sup>45,46</sup> The Si 2p XPS spectrum of  $\text{SiO}_2@\text{MnCo}_2\text{O}_4-1$  (Fig. 4(b)) shows a peak at 102.7 eV, suggesting the presence of  $\text{Si}^{4+}$ . The Mn 2p spectrum of  $\text{SiO}_2@\text{MnCo}_2\text{O}_4-1$  (Fig. 4(b)) exhibits peaks due to Mn 2p<sub>3/2</sub> (642.2 eV ( $\text{Mn}^{2+}$ ) and 644 eV ( $\text{Mn}^{3+}$ ) and Mn 2p<sub>1/2</sub> (654.2 eV ( $\text{Mn}^{3+}$ )). The Co 2p spectrum of  $\text{SiO}_2@\text{MnCo}_2\text{O}_4-1$  (Fig. 4(b)) shows peaks due to Co 2p<sub>3/2</sub> (781.1 eV ( $\text{Co}^{2+}$ ) and 782.7 eV ( $\text{Co}^{3+}$ ) and Co 2p<sub>1/2</sub>

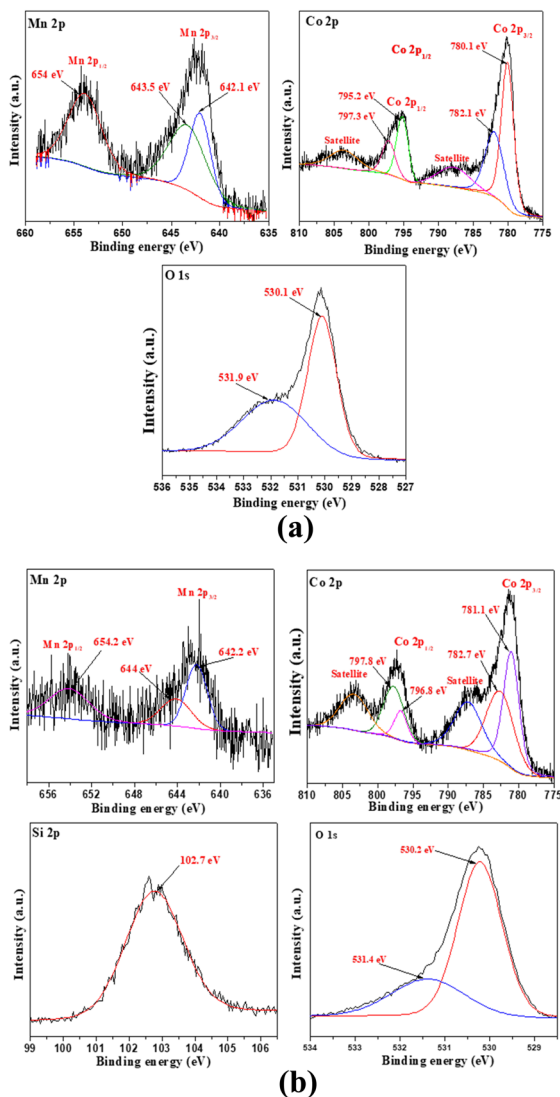


Fig. 4 XPS spectra of (a)  $\text{MnCo}_2\text{O}_4$  NPs and (b)  $\text{SiO}_2@MnCo_2O_4-1$  core-shell nanoparticles calcined at  $500^\circ\text{C}$ .

( $796.8\text{ eV}$  ( $\text{Co}^{2+}$ ) and  $797.8\text{ eV}$  ( $\text{Co}^{3+}$ )). Two satellite peaks are also observed at  $787.5\text{ eV}$  and  $803.5\text{ eV}$ . The O  $1s$  spectrum of  $\text{SiO}_2@MnCo_2O_4-1$  (Fig. 4b) exhibits peaks at  $530.2\text{ eV}$  and  $531.4\text{ eV}$  due to lattice oxygen of  $\text{MnCo}_2\text{O}_4$  and surface hydroxyl oxygen, respectively.<sup>44–46</sup>

### Magnetic properties

Magnetic hysteresis ( $M-H$ ) plots of pure  $\text{MnCo}_2\text{O}_4$  NPs and  $\text{SiO}_2@MnCo_2O_4$  nanorattles were recorded at RT ( $300\text{ K}$ ) and  $5\text{ K}$  up to an applied field of  $40\text{ kOe}$ . The  $M-H$  curves of pure  $\text{MnCo}_2\text{O}_4$  NPs and  $\text{SiO}_2@MnCo_2O_4$  samples ( $\text{SiO}_2@MnCo_2O_4-0.25$ ,  $\text{SiO}_2@MnCo_2O_4-0.5$ , and  $\text{SiO}_2@MnCo_2O_4-1$ ) are shown in Fig. 5. At  $300\text{ K}$ , the absence of hysteresis and negligible coercivity indicate paramagnetic nature of the pure  $\text{MnCo}_2\text{O}_4$  NPs and all the  $\text{SiO}_2@MnCo_2O_4$  samples. Table 3 gives the coercivity and magnetization values of pure  $\text{MnCo}_2\text{O}_4$  NPs and  $\text{SiO}_2@MnCo_2O_4$  samples at  $5\text{ K}$ . At  $5\text{ K}$ , the  $M-H$  hysteresis loop

of the  $\text{MnCo}_2\text{O}_4$  nanoparticles exhibits coercivity of  $5.0\text{ kOe}$  and magnetization of  $6.8\text{ emu g}^{-1}$  ( $@40\text{ kOe}$ ), indicating hard ferromagnetic behavior. At  $5\text{ K}$ , the negligible coercivity and finite magnetization of all the  $\text{SiO}_2@MnCo_2O_4$  samples indicate superparamagnetic behavior. The coercivity values for  $\text{SiO}_2@MnCo_2O_4-0.25$ ,  $\text{SiO}_2@MnCo_2O_4-0.5$ , and  $\text{SiO}_2@MnCo_2O_4-1$  at  $5\text{ K}$  are  $0.05\text{ kOe}$ ,  $0.02\text{ kOe}$ , and  $0.09\text{ kOe}$ , respectively. For  $\text{SiO}_2@MnCo_2O_4-0.25$ ,  $\text{SiO}_2@MnCo_2O_4-0.5$ , and  $\text{SiO}_2@MnCo_2O_4-1$ , the magnetization values ( $@40\text{ kOe}$ ) at  $5\text{ K}$  are  $46.5\text{ emu g}^{-1}$ ,  $36.3\text{ emu g}^{-1}$ , and  $25.5\text{ emu g}^{-1}$ , respectively.

At low temperature, the dominance of magneto-crystalline anisotropy leads to higher coercivity and magnetization of the  $\text{MnCo}_2\text{O}_4$  nanoparticles and  $\text{SiO}_2@MnCo_2O_4$  samples.<sup>47</sup> The lower coercivity of  $\text{SiO}_2@MnCo_2O_4$  nanorattles compared to pure  $\text{MnCo}_2\text{O}_4$  nanoparticles is attributed to the diamagnetic  $\text{SiO}_2$  phase in the nanorattles.<sup>48</sup> The higher magnetization of  $\text{SiO}_2@MnCo_2O_4$  samples compared to pure  $\text{MnCo}_2\text{O}_4$  NPs is attributed to smaller crystallite size of  $\text{MnCo}_2\text{O}_4$  NPs in the  $\text{SiO}_2@MnCo_2O_4$  samples. In the  $\text{MnCo}_2\text{O}_4$  nanoparticles,  $\text{SiO}_2@MnCo_2O_4-0.25$ ,  $\text{SiO}_2@MnCo_2O_4-0.5$ , and  $\text{SiO}_2@MnCo_2O_4-1$ , the crystallite size of  $\text{MnCo}_2\text{O}_4$  are  $9.3\text{ nm}$ ,  $6.4\text{ nm}$ ,  $3.5\text{ nm}$ , and  $7.5\text{ nm}$ , respectively. The ZFC and FC magnetization curves recorded under  $2\text{ kOe}$  for pure  $\text{MnCo}_2\text{O}_4$  NPs and  $\text{SiO}_2@MnCo_2O_4$  nanorattles ( $\text{SiO}_2@MnCo_2O_4-0.25$ ,  $\text{SiO}_2@MnCo_2O_4-0.5$ , and  $\text{SiO}_2@MnCo_2O_4-1$ ) are shown in Fig. 6. The ZFC and FC curves of pure  $\text{MnCo}_2\text{O}_4$  NPs display a bifurcation at about  $100\text{ K}$  and a hump at  $25\text{ K}$ , which are assigned as irreversible temperature ( $T_{\text{irr}}$ ) and blocking temperature ( $T_{\text{B}}$ ), respectively. All the  $\text{SiO}_2@MnCo_2O_4$  core-shell nanorattles show overlapped ZFC and FC curves without any hump, indicating superparamagnetic nature of the samples despite the absence of a maximum in the ZFC curve. The absence of maxima in the ZFC curves of the  $\text{SiO}_2@MnCo_2O_4$  samples is due to the absence of ferrimagnetic ordering in these samples.<sup>49–52</sup>

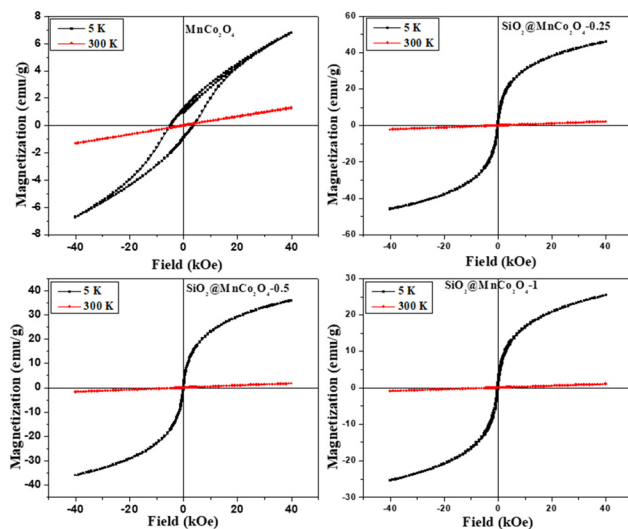


Fig. 5  $M-H$  curves for  $\text{MnCo}_2\text{O}_4$  NPs and  $\text{SiO}_2@MnCo_2O_4$  core-shell nanorattles at  $300\text{ K}$  and  $5\text{ K}$ .

**Table 3** Summary of magnetic parameters of  $\text{MnCo}_2\text{O}_4$  NPs and  $\text{SiO}_2@\text{MnCo}_2\text{O}_4$  core-shell NPs at 5 K

Sample code	Coercivity ( $H_c$ , kOe)	Magnetization ( $\text{emu g}^{-1}$ )	Crystallite size (nm)
$\text{MnCo}_2\text{O}_4$	5.00	6.8	9.3
$\text{SiO}_2@\text{MnCo}_2\text{O}_4-0.25$	0.05	46.5	6.4
$\text{SiO}_2@\text{MnCo}_2\text{O}_4-0.5$	0.02	36.3	3.5
$\text{SiO}_2@\text{MnCo}_2\text{O}_4-1$	0.09	25.5	7.5

### Peroxidase-like activity of $\text{SiO}_2@\text{MnCo}_2\text{O}_4$ nanorattles

The current study demonstrates the peroxidase-like activity of pure  $\text{MnCo}_2\text{O}_4$  nanoparticles and  $\text{SiO}_2@\text{MnCo}_2\text{O}_4$  core-shell nanorattles ( $\text{SiO}_2@\text{MnCo}_2\text{O}_4-0.25$ ,  $\text{SiO}_2@\text{MnCo}_2\text{O}_4-0.5$ , and  $\text{SiO}_2@\text{MnCo}_2\text{O}_4-1$ ). The  $\text{SiO}_2@\text{MnCo}_2\text{O}_4$  core-shell nanorattles were tested as catalyst for peroxidase-like activity using TMB and  $\text{H}_2\text{O}_2$  as substrate and oxidizing agent, respectively. The oxidation of TMB using  $\text{SiO}_2@\text{MnCo}_2\text{O}_4$  core-shell nanorattles in the presence of  $\text{H}_2\text{O}_2$  leads to formation of  $\text{TMB}^{*+}$  (blue-colored charge transfer complex). The UV-Vis spectrum of  $\text{TMB}^{*+}$  consists of a characteristic absorption maximum at 652 nm.<sup>28</sup> An intense blue-colored solution is obtained using  $\text{SiO}_2@\text{MnCo}_2\text{O}_4$  as the catalyst compared to pure  $\text{MnCo}_2\text{O}_4$  NPs, which suggests the role of  $\text{SiO}_2@\text{MnCo}_2\text{O}_4$  as the catalyst in peroxidase-like activity.

The UV-Vis spectral results (abs. vs. time plots) and % relative efficiency of peroxidase-like activity for pure  $\text{MnCo}_2\text{O}_4$  NPs and  $\text{SiO}_2@\text{MnCo}_2\text{O}_4$  core-shell NPs are shown in Fig. 7 and Fig. S14 (ESI<sup>†</sup>), respectively. As shown in Fig. 7, compared to pure  $\text{MnCo}_2\text{O}_4$  nanoparticles,  $\text{SiO}_2@\text{MnCo}_2\text{O}_4$  nanorattles show better peroxidase-like activity.  $\text{SiO}_2@\text{MnCo}_2\text{O}_4-1$  exhibits the best peroxidase-like activity among the  $\text{SiO}_2@\text{MnCo}_2\text{O}_4$  samples.

### Influence of physicochemical conditions on the peroxidase-like activity

In the current study, various experimental parameters were varied to achieve optimal conditions for the peroxidase-like

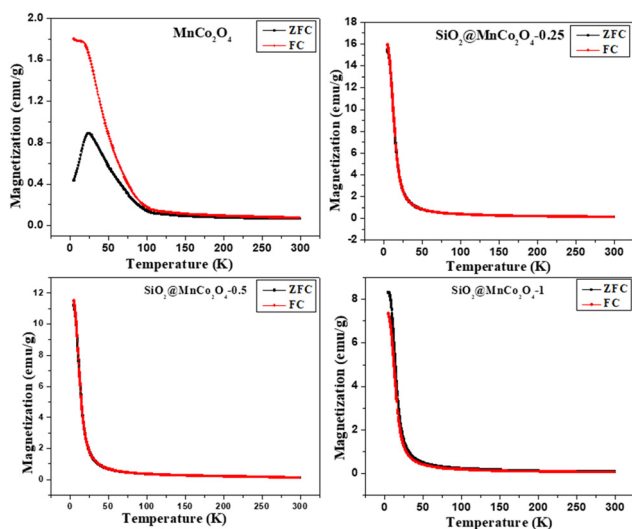


**Fig. 6** ZFC and FC curves for  $\text{MnCo}_2\text{O}_4$  NPs and  $\text{SiO}_2@\text{MnCo}_2\text{O}_4$  core-shell nanorattles.

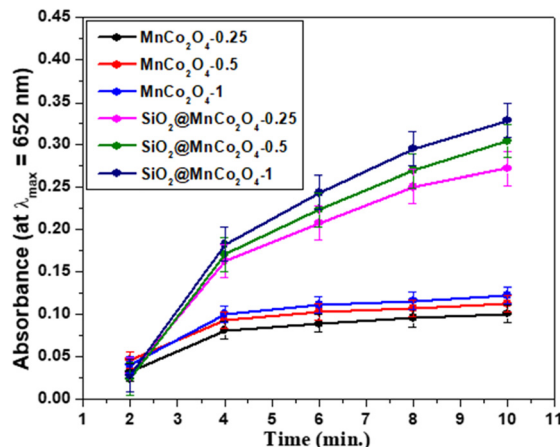


**Fig. 7** Peroxidase-like activity of  $\text{MnCo}_2\text{O}_4$  NPs and  $\text{SiO}_2@\text{MnCo}_2\text{O}_4$  core-shell nanorattles as indicated by time dependent absorbance.

activity of the  $\text{SiO}_2@\text{MnCo}_2\text{O}_4$  core-shell nanorattles. Studies were carried out to investigate the effect of varying pH (2–12) and amount of catalyst (5  $\mu\text{L}$  – 60  $\mu\text{L}$  of dispersion) on the peroxidase-like activity of the  $\text{SiO}_2@\text{MnCo}_2\text{O}_4$  core-shell nanorattles. The influence of varying pH (2–12) on the peroxidase-like activity (Fig. S15(a), ESI<sup>†</sup>) reveals the maximum peroxidase-like activity of  $\text{SiO}_2@\text{MnCo}_2\text{O}_4$  core-shell nanorattles at pH = 5. At low pH (<5), protonation of amino groups of TMB occurs. The protonation of amino groups leads to the retardation of electron transfer from the substrate (TMB) to the catalyst surface ( $\text{SiO}_2@\text{MnCo}_2\text{O}_4-1$ ). Hence, in a strongly acidic medium, the peroxidase-like activity of  $\text{SiO}_2@\text{MnCo}_2\text{O}_4-1$  decreases. When pH > 5, production of  $\text{O}_2$  and  $\text{H}_2\text{O}$  occurs *via* the break-down of  $\text{H}_2\text{O}_2$  in the presence of more hydroxyl ions, which leads to suppression of the peroxidase-like activity of  $\text{SiO}_2@\text{MnCo}_2\text{O}_4-1$ .<sup>53,54</sup> A linear variation of the peroxidase-like activity of  $\text{SiO}_2@\text{MnCo}_2\text{O}_4-1$  with an increment in catalyst dose from 5  $\mu\text{L}$  to 60  $\mu\text{L}$  of dispersion (1 mg catalyst dispersed by sonication in 1 mL  $\text{H}_2\text{O}$ ) is observed (Fig. S15(b), ESI<sup>†</sup>). A leaching experiment was carried out to understand further the peroxidase-like activity of  $\text{SiO}_2@\text{MnCo}_2\text{O}_4-1$ . In a typical experiment,  $\text{SiO}_2@\text{MnCo}_2\text{O}_4-1$  (30  $\mu\text{L}$  dispersion) was incubated in 3 mL buffer (pH = 5) for about 30 minutes. The supernatant solution obtained by centrifugation was further examined for peroxidase-like activity by adding TMB and  $\text{H}_2\text{O}_2$  solutions. The UV-Vis spectrum of the leached solution was recorded in kinetic mode up to 10 minutes (Fig. S16, ESI<sup>†</sup>). The negligible absorbance shown by the leached solution confirms the role of  $\text{MnCo}_2\text{O}_4$  NPs in the peroxidase-like activity and the activity is not due to leached ions.

### Kinetic studies

Steady state-kinetic studies on the peroxidase-like activity of  $\text{SiO}_2@\text{MnCo}_2\text{O}_4-1$  nanorattles were performed using different substrates (*i.e.*, TMB and  $\text{H}_2\text{O}_2$ ). The kinetic results at different TMB concentrations by fixing  $\text{H}_2\text{O}_2$  concentration and *vice versa* are shown in Fig. S17(a and b) (ESI<sup>†</sup>). The kinetic parameters ( $K_m$  and  $V_{\text{max}}$ ) were determined from the slope and

intercept values of Lineweaver–Burk reciprocal plots (Fig. S18(a and b), ESI†). The  $K_m$  and  $V_{max}$  values for  $\text{SiO}_2@\text{MnCo}_2\text{O}_4$ -1 core–shell nanorattles are summarized in Table 4. Table 4 also gives the kinetic parameters for different metal oxide nanoparticles and core–shell NPs reported in the literature.<sup>5,54–60</sup> The Michaelis–Menten constant ( $K_m$ ) is inversely proportional to the catalyst's affinity towards a substrate; a smaller  $K_m$  value indicates higher affinity of a catalyst towards the substrate.<sup>54</sup> The  $K_m$  and  $V_{max}$  values for  $\text{SiO}_2@\text{MnCo}_2\text{O}_4$ -1 core–shell nanorattles towards TMB are 0.032 mM and  $1.596 \times 10^{-8} \text{ Ms}^{-1}$ , respectively. The  $K_m$  and  $V_{max}$  values for  $\text{SiO}_2@\text{MnCo}_2\text{O}_4$ -1 core–shell nanorattles towards  $\text{H}_2\text{O}_2$  are 2.7 mM and  $0.532 \times 10^{-8} \text{ Ms}^{-1}$ , respectively. The reported  $K_m$  and  $V_{max}$  values for  $\text{MnCo}_2\text{O}_4$  nanoparticles towards TMB are 0.063 mM and  $2.17 \times 10^{-5} \text{ Ms}^{-1}$ , respectively.<sup>51</sup> For the natural peroxidase enzyme (HRP), the reported  $K_m$  and  $V_{max}$  values towards TMB are 0.434 mM and  $10 \times 10^{-8} \text{ Ms}^{-1}$  and towards  $\text{H}_2\text{O}_2$ , the values are 3.70 mM and  $8.71 \times 10^{-8} \text{ Ms}^{-1}$ , respectively.<sup>55</sup> The observed  $K_m$  value for  $\text{SiO}_2@\text{MnCo}_2\text{O}_4$ -1 nanorattles towards TMB, in the present study, is smaller than that of  $\text{MnCo}_2\text{O}_4$  nanoparticles and natural peroxidase enzyme (HRP). These results indicate high affinity of  $\text{SiO}_2@\text{MnCo}_2\text{O}_4$ -1 core–shell nanorattles towards TMB with better peroxidase-like activity.

#### Mechanism of peroxidase-like activity of $\text{SiO}_2@\text{MnCo}_2\text{O}_4$ nanorattles

Fig. 8 shows the mechanism for the peroxidase-like activity of  $\text{SiO}_2@\text{MnCo}_2\text{O}_4$  nanorattles. In the first step, adsorption of tetramethylbenzidine (TMB) molecules occurs on the surface of  $\text{SiO}_2@\text{MnCo}_2\text{O}_4$  nanorattles. This promotes nitrogen electron pair donation from the  $\text{NH}_2$  groups of TMB towards the surface of  $\text{SiO}_2@\text{MnCo}_2\text{O}_4$ , resulting in high electron density over  $\text{SiO}_2@\text{MnCo}_2\text{O}_4$ .<sup>31,54,61</sup> The  $\text{SiO}_2@\text{MnCo}_2\text{O}_4$  core–shell nanorattles reduce  $\text{H}_2\text{O}_2$  into  $\text{OH}^-$  and  $\text{OH}^\bullet$  species. The  $\text{OH}^-$  and  $\text{OH}^\bullet$  species facilitate the oxidation of TMB into  $\text{TMB}^{\bullet+}$  (a blue-colored CT complex). The rattle-like hierarchical structure of  $\text{MnCo}_2\text{O}_4$  NPs present on the surface of  $\text{SiO}_2$  spheres eases

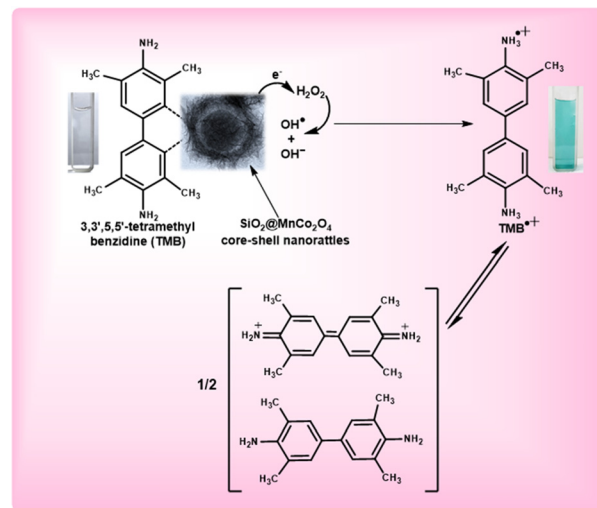


Fig. 8 Proposed mechanism of peroxidase-like activity of  $\text{SiO}_2@\text{MnCo}_2\text{O}_4$  core–shell nanorattles using TMB as a substrate.

interaction between tetramethylbenzidine and the catalytic active centers ( $\text{Mn}^{2+}$  and  $\text{Co}^{2+}$ ) leading to improved peroxidase-like activity of the  $\text{SiO}_2@\text{MnCo}_2\text{O}_4$  nanorattles.

In the current study, high surface area and rattle-like morphology of  $\text{SiO}_2@\text{MnCo}_2\text{O}_4$  lead to enhanced peroxidase-like activity. The higher peroxidase-like activity of  $\text{SiO}_2@\text{MnCo}_2\text{O}_4$ -1 compared to the other samples is attributed to its high surface area ( $356 \text{ m}^2 \text{ g}^{-1}$ ). The  $\text{SiO}_2@\text{MnCo}_2\text{O}_4$  core–shell nanorattles, synthesized in the current study, exhibit high surface area due to their rattle-type porous morphology. The high surface area of the  $\text{SiO}_2@\text{MnCo}_2\text{O}_4$  core–shell nanorattles is helpful for enhanced peroxidase-like activity. The rattle-type porous nature of hierarchical  $\text{MnCo}_2\text{O}_4$  NPs on the surface of  $\text{SiO}_2$  spheres provides less steric hindrance for the TMB molecules to interact with the catalytic centres ( $\text{Mn}^{2+}$  and  $\text{Co}^{2+}$ ).<sup>62,63</sup> This promotes electron transfer from the  $\text{SiO}_2@\text{MnCo}_2\text{O}_4$  core–shell nanorattles towards  $\text{H}_2\text{O}_2$  resulting in faster chemical reduction of  $\text{H}_2\text{O}_2$ .

Fig. S19 (ESI†) shows the fluorescence spectra for the detection of  $\text{OH}^\bullet$  radicals produced during the peroxidase-like activity. Terephthalic acid (probe molecule,  $\lambda_{\text{exc}} = 315 \text{ nm}$ ) produces fluorescent 2-hydroxyterephthalic acid ( $\lambda_{\text{em}} = 425 \text{ nm}$ ) on reacting with hydroxyl radicals. It can be noted that the fluorescence intensity increases with time due to increasing production of hydroxyl radicals. The PL results suggest the role of hydroxyl radicals in the peroxidase-like activity of  $\text{SiO}_2@\text{MnCo}_2\text{O}_4$  nanorattles.

#### Detection of $\text{H}_2\text{O}_2$ using $\text{SiO}_2@\text{MnCo}_2\text{O}_4$ nanorattles

$\text{SiO}_2@\text{MnCo}_2\text{O}_4$  core–shell nanorattles were used for the detection of  $\text{H}_2\text{O}_2$  using peroxidase-like activity. A calibration plot (Fig. S20, ESI†) was recorded for  $\text{SiO}_2@\text{MnCo}_2\text{O}_4$ -1 with varying concentration of  $\text{H}_2\text{O}_2$  (linear range = 0.05 mM to 1 mM). The equation given below was used for determining the limit of detection (LOD) of  $\text{H}_2\text{O}_2$ .

Table 4 Comparison of steady-state kinetic parameters ( $K_m$  and  $V_{max}$ ) for  $\text{SiO}_2@\text{MnCo}_2\text{O}_4$  core–shell nanorattles with those reported in the literature

Catalyst	Substrate	$K_m$ (mM)	$V_{max}$ ( $\text{Ms}^{-1}$ )	Reference
$\text{SiO}_2@\text{Co}_3\text{O}_4$ CSNPs	TMB	0.087	$0.012 \times 10^{-8}$	5
$\text{SiO}_2@\text{Co}_3\text{O}_4$ CSNPs	$\text{H}_2\text{O}_2$	25.2	$0.015 \times 10^{-8}$	5
$\text{MnCo}_2\text{O}_4$ nanoparticles	TMB	0.063	$2.17 \times 10^{-5}$	54
HRP	TMB	0.434	$10.0 \times 10^{-8}$	54
HRP	$\text{H}_2\text{O}_2$	3.70	$8.71 \times 10^{-8}$	55
$\text{MnO}_2$ nanoparticles	TMB	0.04	$5.78 \times 10^{-6}$	56
$\text{Co}_3\text{O}_4$ nanoparticles	TMB	0.037	$6.27 \times 10^{-8}$	57
$\text{Co}_3\text{O}_4$ nanoparticles	$\text{H}_2\text{O}_2$	140.07	$12.1 \times 10^{-8}$	57
$\text{Co}_3\text{O}_4@\text{NiO}$ CSNPs	TMB	0.036	—	58
$\text{Co}_3\text{O}_4@\text{NiO}$ CSNPs	$\text{H}_2\text{O}_2$	8.17	—	58
$\text{Fe}_3\text{O}_4@\text{CoFe-LDH}$	TMB	0.395	—	59
$\text{Fe}_3\text{O}_4@\text{CoFe-LDH}$	$\text{H}_2\text{O}_2$	47.6	—	59
$\text{TiO}_2@\text{CeO}_x$	TMB	0.28	$6.5 \times 10^{-9}$	60
$\text{TiO}_2@\text{CeO}_x$	$\text{H}_2\text{O}_2$	6.29	$34 \times 10^{-9}$	60
$\text{SiO}_2@\text{MnCo}_2\text{O}_4$ -1	TMB	0.032	$1.596 \times 10^{-8}$	This work
$\text{SiO}_2@\text{MnCo}_2\text{O}_4$ -1	$\text{H}_2\text{O}_2$	2.7	$0.532 \times 10^{-8}$	This work



Limit of detection =  $3 \times$  (Standard deviation due to blank/  
Slope)

The standard deviation was estimated by recording the absorption spectra of a blank solution (*i.e.*  $[\text{H}_2\text{O}_2] = 0$ ) three times. The slope was calculated from the absorbance ( $@\lambda_{\text{max}} = 652 \text{ nm}$ ) versus  $[\text{H}_2\text{O}_2]$  plot (Fig. S20(b), ESI<sup>†</sup>). The estimated LOD value for  $\text{H}_2\text{O}_2$  using  $\text{SiO}_2@\text{MnCo}_2\text{O}_4$  core-shell nanorattles is 0.083 mM and it is comparable with that reported in the literature.<sup>58,63</sup>

## Conclusions

The current work demonstrates a simple and cost-effective synthetic strategy to synthesize  $\text{SiO}_2@\text{MnCo}_2\text{O}_4$  core-shell nanorattles *via* calcination of  $\text{SiO}_2@\text{MnCo-LDH}$  precursors at 500 °C.  $\text{MnCo}_2\text{O}_4$  NPs deposit on the surface of  $\text{SiO}_2$  spheres creating a hollow space (void) between the core and shell. The  $[\text{Mn}^{2+}:\text{Co}^{2+}]$  ratio affects thickness of the  $\text{MnCo}_2\text{O}_4$  shell and void distance between the core ( $\text{SiO}_2$ ) and the shell ( $\text{MnCo}_2\text{O}_4$ ). XRD results confirm the formation of  $\text{MnCo}_2\text{O}_4$  NPs in the  $\text{SiO}_2@\text{MnCo}_2\text{O}_4$  samples. FESEM and TEM analyses show nanorattle-like morphology of all the  $\text{SiO}_2@\text{MnCo}_2\text{O}_4$  samples. The mean shell thickness and void distance between the  $\text{SiO}_2$  core and  $\text{MnCo}_2\text{O}_4$  shell in the  $\text{SiO}_2@\text{MnCo}_2\text{O}_4$  core-shell nanorattles vary from  $38 \pm 8 \text{ nm}$  to  $60 \pm 12 \text{ nm}$  and  $16 \pm 3 \text{ nm}$  to  $30 \pm 6 \text{ nm}$ , respectively. BET measurements indicate higher surface area of  $\text{SiO}_2@\text{MnCo}_2\text{O}_4$  core-shell nanorattles ( $278 \text{ m}^2 \text{ g}^{-1}$  to  $356 \text{ m}^2 \text{ g}^{-1}$ ) compared to the constituents. XPS analysis confirms the presence of  $\text{Si}^{4+}$ ,  $\text{Mn}^{2+}$ ,  $\text{Co}^{2+}$ ,  $\text{Mn}^{3+}$ ,  $\text{Co}^{3+}$ , and  $\text{O}^{2-}$  in the  $\text{SiO}_2@\text{MnCo}_2\text{O}_4$  nanorattles. Magnetic measurements indicate paramagnetic and superparamagnetic behavior of  $\text{SiO}_2@\text{MnCo}_2\text{O}_4$  nanorattles at 300 K and 5 K, respectively. The  $\text{SiO}_2@\text{MnCo}_2\text{O}_4$  nanorattles exhibit better peroxidase-like activity than pure  $\text{MnCo}_2\text{O}_4$  NPs and horseradish peroxidase. The peroxidase-like activity of the core-shell nanorattles can be useful for several sensing applications, such as the detection of glucose,  $\text{H}_2\text{O}_2$ , ascorbic acid, hydroquinone, protein, and dopamine.

## Conflicts of interest

There are no conflicts of interest to declare.

## Acknowledgements

Pankaj Rana expresses his gratitude to the UGC and the Ministry of Education, Government of India for awarding him a fellowship (JRF/SRF). The authors express gratitude to Institute Instrumentation Centre (IIC), IIT Roorkee for providing the necessary instrumentation facilities. The authors are also thankful to the Department of Metallurgical and Materials Engineering, IIT Roorkee for providing the TEM facility.

## References

- 1 A. M. El-Toni, M. A. Habila, J. P. Labis, Z. A. Allothman, M. Alhoshan, A. A. Elzatahry and F. Zhang, *Nanoscale*, 2016, **8**, 2510–2531.
- 2 M. Priebe and K. M. Fromm, *Chem. – Eur. J.*, 2015, **21**, 3854–3874.
- 3 J. Liu, R. Harrison, J. Z. Zhou, T. T. Liu, C. Yu, G. Q. Lu, S. Z. Qiao and Z. P. Xu, *J. Mater. Chem.*, 2011, **21**, 10641–10644.
- 4 J. Lee, J. C. Park and H. Song, *Adv. Mater.*, 2008, **20**, 1523–1528.
- 5 S. Kandula and P. Jeevanandam, *RSC Adv.*, 2015, **5**, 5295–5306.
- 6 J. S. Chen, C. M. Li, W. W. Zhou, Q. Y. Yan, L. A. Archer and X. W. Lou, *Nanoscale*, 2009, **1**, 280–285.
- 7 A. Rokicinska, M. Zurowska, P. Łatka and P. Kustrowski, *Catalysts*, 2021, **11**, 1097.
- 8 Y. Hu, X. T. Zheng, J. S. Chen, M. Zhou, C. M. Li and X. W. Lou, *J. Mater. Chem.*, 2011, **21**, 8052–8056.
- 9 B. J. Jankiewicz, D. Jamiola, J. Choma and M. Jaroniec, *Adv. Colloid Interface Sci.*, 2012, **170**, 28–47.
- 10 N. Yan, Z. Zhao, Y. Li, F. Wang, H. Zhong and Q. Chen, *Inorg. Chem.*, 2014, **53**, 9073–9079.
- 11 Y. Yu, M. Zhou, W. Zhang, L. Huang, D. Miao, H. Zhu and G. Su, *Mol. Pharmaceutics*, 2019, **16**, 1929–1938.
- 12 C. Liu, J. Li, J. Qi, J. Wang, R. Luo, J. Shen, X. Sun, W. Han and L. Wang, *ACS Appl. Mater. Interfaces*, 2014, **6**, 13167–13173.
- 13 T. Zhang, Z. Li, L. Wang, P. Sun, Z. Zhang and S. Wang, *ChemSusChem*, 2018, **11**, 2730–2736.
- 14 T. Pettong, P. Iamprasertkun, A. Krittayavathananon, P. Sukha, P. Sirisinudomkit, A. Seubsai, M. Chareonpanich, P. Kongkachuichay, J. Limtrakul and M. Sawangphruk, *ACS Appl. Mater. Interfaces*, 2016, **8**, 34045–34053.
- 15 B. Wang, S. Wang, Y. Tang, C. W. Tsang, J. Dai, M. K. H. Leung and X. Y. Lu, *Appl. Energy*, 2019, **252**, 113452.
- 16 W. Yang, J. Hao, Z. Zhang, B. Lu, B. Zhang and J. Tang, *Catal. Commun.*, 2014, **46**, 174–178.
- 17 S. Tarighi and N. M. Juibari, *ChemistrySelect*, 2019, **4**, 6506–6515.
- 18 Y. Liang, H. Wang, J. Zhou, Y. Li, J. Wang, T. Regier and H. Dai, *J. Am. Chem. Soc.*, 2012, **134**, 3517–3523.
- 19 X. Wang, L. Xu, K. Song, R. Yang, L. Jia, X. Guo, X. Jing and J. Wang, *Colloids Surf., A*, 2019, **570**, 73–80.
- 20 Y. Zhao, L. Hu, S. Zhao and L. Wu, *Adv. Funct. Mater.*, 2016, **26**, 4085–4093.
- 21 Z. Li, S. Liu, L. Li, W. Qi, W. Lai, L. Li, X. Zhao, Y. Zhang and W. Zhang, *Sol. Energy Mater. Sol. Cells*, 2021, **220**, 110859.
- 22 C. Sun, J. Yang, Z. Dai, X. Wang, Y. Zhang, L. Li, P. Chen, W. Huang and X. Dong, *Nano Res.*, 2016, **9**, 1300–1309.
- 23 L. Zhao, M. Yang, Z. Zhang, Y. Ji, Y. Teng, Y. Feng and X. Liu, *Inorg. Chem. Commun.*, 2018, **89**, 22–26.
- 24 J. A. A. Mehrez, K. A. Owusu, Q. Chen, L. Li, K. Hamwi, W. Luo and L. Mai, *Inorg. Chem. Front.*, 2019, **6**, 857–865.
- 25 L. Wang, Y. Min, D. Xu, F. Yu, W. Zhou and A. Cuschieri, *Chem. Commun.*, 2014, **50**, 11147–11150.

- 26 Y. C. Yang, Y. T. Wang and W. L. Tseng, *ACS Appl. Mater. Interfaces*, 2017, **9**, 10069–10077.
- 27 Z. Chen, J. J. Yin, Y. T. Zhou, Y. Zhang, L. Song, M. Song, S. Hu and N. Gu, *ACS Nano*, 2012, **6**, 4001–4012.
- 28 J. Mu, Y. Wang, M. Zhao and L. Zhang, *Chem. Commun.*, 2012, **48**, 2540–2542.
- 29 W. Chen, J. Chen, Y. Bin Feng, L. Hong, Q. Y. Chen, L. F. Wu, X. H. Lin and X. H. Xia, *Analyst*, 2012, **137**, 1706–1712.
- 30 S. Fu, S. Wang, X. Zhang, A. Qi, Z. Liu, X. Yu, C. Chen and L. Li, *Colloids Surf., B*, 2017, **154**, 239–245.
- 31 M. Gao, X. Lu, M. Chi, S. Chen and C. Wang, *Inorg. Chem. Front.*, 2017, **4**, 1862–1869.
- 32 Y. Ma, M. Zhu, Q. He, M. Zhao and H. Cui, *ACS Sustainable Chem. Eng.*, 2022, **10**, 5651–5658.
- 33 L. Zhang, P. Hu, X. Zhao, R. Tian, R. Zou and D. Xia, *J. Mater. Chem.*, 2011, **21**, 18279–18283.
- 34 G. Gao, H. B. Wu, S. Ding and X. W. Lou, *Small*, 2015, **11**, 432–436.
- 35 S. Kandula and P. Jeevanandam, *Eur. J. Inorg. Chem.*, 2015, 4260–4274.
- 36 W. Stober, A. Fink and E. Bohn, *J. Colloid Interface Sci.*, 1968, **26**, 62–69.
- 37 P. Yang, F. Wang, X. Luo, Y. Zhang, J. Guo, W. Shi and C. Wang, *ACS Appl. Mater. Interfaces*, 2014, **6**, 12581–12587.
- 38 J. Xu, J. Liu, R. Che, C. Liang, M. Cao, Y. Li and Z. Liu, *Nanoscale*, 2014, **6**, 5782–5790.
- 39 L. Kumar, H. Chauhan, N. Yadav, N. Yadav, S. A. Hashmi and S. Deka, *ACS Appl. Energy Mater.*, 2018, **1**, 6999–7006.
- 40 S. Liu, S. C. Lee, U. Patil, I. Shackery, S. Kang, K. Zhang, J. H. Park, K. Y. Chung and S. Chan Jun, *J. Mater. Chem. A*, 2017, **5**, 1043–1049.
- 41 J. Yan, Z. Fan, W. Sun, G. Ning, T. Wei, Q. Zhang, R. Zhang, L. Zhi and F. Wei, *Adv. Funct. Mater.*, 2012, **22**, 2632–2641.
- 42 N. Y. Tashkandi and R. M. Mohamed, *Ceram. Int.*, 2022, **48**, 13216–13228.
- 43 P. Prieto, J. F. Marco, A. Serrano, M. Manso and J. de la Figuera, *J. Alloys Compd.*, 2019, **810**, 151912.
- 44 J. Mahajan and P. Jeevanandam, *Mater. Today Commun.*, 2021, **26**, 102085.
- 45 S. Wang, Y. Hou and X. Wang, *ACS Appl. Mater. Interfaces*, 2015, **7**, 4327–4335.
- 46 R. Huang, J. Lin, J. Zhou, E. Fan, X. Zhang, R. Chen, F. Wu and L. Li, *Small*, 2021, **17**, 1–9.
- 47 F. M. M. Borges, D. M. A. Melo, M. S. A. Câmara, A. E. Martinelli, J. M. Soares, J. H. de Araújo and F. A. O. Cabral, *J. Magn. Magn. Mater.*, 2006, **302**, 273–277.
- 48 S. K. Yadav and P. Jeevanandam, *J. Nanoparticle Res.*, 2016, **18**, 1–25.
- 49 M. Iacob, D. Sirbu, C. Tugui, G. Stiubianu, L. Sacarescu, V. Cozan, A. Zeleňáková, E. Čižmár, A. Feher and M. Cazacu, *RSC Adv.*, 2015, **5**, 62563–62570.
- 50 T. H. Dolla, K. Pruessner, D. G. Billing, C. Sheppard, A. Prinsloo and P. Ndungu, *Mater. Today Proc.*, 2018, **5**, 10488–10495.
- 51 P. Pramanik, S. Thota, S. Singh, D. C. Joshi, B. Weise, A. Waske and M. S. Seehra, *J. Phys.: Condens. Matter*, 2017, **29**, 425803.
- 52 Y. He, N. Li, W. Li, X. Zhang, X. Zhang, Z. Liu and Q. Liu, *Sens. Actuators, B*, 2021, **326**, 128850.
- 53 X. Zhao, S. Zhao, S. Li, X. Yao, X. Zhu, W. Chen, G. Fan, Z. Liu, Q. Liu and K. Yue, *ACS Appl. Nano Mater.*, 2021, **4**, 8706–8715.
- 54 E. Ding, J. Hai, F. Chen and B. Wang, *ACS Appl. Nano Mater.*, 2018, **1**, 4156–4163.
- 55 X. Q. Zhang, S. W. Gong, Y. Zhang, T. Yang, C. Y. Wang and N. Gu, *J. Mater. Chem.*, 2010, **20**, 5110–5116.
- 56 X. Liu, Q. Wang, H. Zhao, L. Zhang, Y. Su and Y. Lv, *Analyst*, 2012, **137**, 4552–4558.
- 57 J. Dong, L. Song, J. J. Yin, W. He, Y. Wu, N. Gu and Y. Zhang, *ACS Appl. Mater. Interfaces*, 2014, **6**, 1959–1970.
- 58 Y. Zhu, Z. Yang, M. Chi, M. Li, C. Wang and X. Lu, *Talanta*, 2018, **181**, 431–439.
- 59 W. Yang, J. Li, M. Wang, X. Sun, Y. Liu, J. Yang and D. H. L. Ng, *Colloids Surf., B*, 2020, **188**, 110742.
- 60 L. Artiglia, S. Agnoli, M. C. Paganini, M. Cattelan and G. Granozzi, *ACS Appl. Mater. Interfaces*, 2014, **6**, 20130–20136.
- 61 J. Mu, L. Zhang, G. Zhao and Y. Wang, *Phys. Chem. Chem. Phys.*, 2014, **16**, 15709–15716.
- 62 L. Huang, K. Chen, W. Zhang, W. Zhu, X. Liu, J. Wang, R. Wang, N. Hu, Y. Suo and J. Wang, *Sens. Actuators, B*, 2018, **269**, 79–87.
- 63 W. Huang, T. Lin, Y. Cao, X. Lai, J. Peng and J. Tu, *Sensors*, 2017, **17**, 217–228.